Complex Landau levels and related transport properties in the strained zigzag graphene nanoribbons

Zhi-qiang Bao [1,*] Ju-wen Ding [1] and Junjie Qi [2,†]
[1]*Key Laboratory of Polar Materials and Devices (MOE), Department of Electronics, East China Normal University, Shanghai 200241, China*
[2]*Beijing Academy of Quantum Information Sciences, Beijing 100193, China*

(Received 14 October 2022; accepted 6 March 2023; published 15 March 2023)

The real magnetic fields (MFs) acting on graphene can induce flat real Landau levels (LLs). As an analogy, strains in graphene can produce significant pseudo MFs, triggering the appearance of dispersive pseudo LLs. By analyzing the low-energy effective Hamiltonian, we introduce the concept of the effective orbital MFs to integrate the real MFs and pseudo MFs. Accordingly, we obtain the complex LLs which incorporate the real LLs and pseudo LLs, and calculate the related transport properties. These concepts enable us to uncover the mechanisms driving the fragility of pseudo LLs against disorders and dephasing, proving that tuning the real MFs and Fermi energy can effectively improve the robust performances. Furthermore, the tunability of the valley-polarized currents is also studied, opening up new possibilities for the design of valleytronics devices.

DOI: 10.1103/PhysRevB.107.125411

I. INTRODUCTION

Unique in two dimensions, graphene possesses two nonequivalent Dirac points, K and K', which leads to the valley degree of freedom [1,2]. The two main edge types of graphene nanoribbons (GNRs), which are basically one-dimensional structures cut from graphene, are zigzag edges and armchair edges. The contrast between the K and K' valleys in the k spaces is one of the primary differences between the zigzag GNRs (ZGNRs) and armchair GNRs (AGNRs). Without intervalley scattering, the K and K' valleys are separated and decoupled specifically for the ZGNRs in the low-energy limit, making the study of valley transport pertinent. However, the K and K' valleys for the AZNRs are both projected to the k space Γ point, indicating that they are not suitable for creating valleytronic devices [3–5]. As a result, we concentrated mostly on the ZGNRs in this work. The ability of ZGNRs to generate pseudomagnetic fields (PMFs) through strains, which in turn leads to the appearance of pseudo-Landau levels (PLLs), is another remarkable property of the material [5–11]. This phenomenon has been identified in several noteworthy investigations [12–15]. Moreover, several experimental studies have shown that graphene can resist nondestructively reversible deformations up to high values of 25%–27% [16–19], implying that it could be a promising material for building novel straintronic devices with the exceptional features associated with PMFs.

A two-terminal ZGNR with the uniaxial strain is shown in Fig. 1(a). The uniaxial strain of the ZGNR is extended along the y direction. Accordingly, the hopping coefficients along the y direction $t_y(n)$ are assumed to be a linear function of n ($n = 1, 2, ..., N_y - 1$). Meanwhile, the hopping coefficients along the x direction are considered to be constant [5,20–22]. As a result, this strain pattern is referred to as the monotonic increasing strain (MIS) [23], which leads to the emergence of a uniform perpendicular PMF. Valley-polarized currents for the K and K' valleys are theoretically predicted in the ZGNRs under the influence of the PMFs [20]. Figure 1(b) shows the K and K' valleys of the strained GNRs in the real magnetic fields (RMFs). As discussed in Sec. IV A, the joint effects of the PMFs and RMFs cause the K' (K) valley to sink (raise) and get narrower (wider). Both the RMFs and PMFs can produce LLs, however, the former results in flat LLs while the latter results in dispersive ones. Additionally, it is shown by the transport characteristics research that the states associated with PLLs and RLLs have distinct robust responses to Anderson disorders and dephasing effects. We offer the idea of the effective orbital magnetic fields (EOMFs), which result in the creation of complex LLs (CLLs), to combine the impacts of RMFs and PMFs to explain the transport characteristics of the strained ZGNRs. We propose several mechanisms of the intervalley and intravalley to explain the distinct robust performances for the RLLs and PLLs, and point out that the valley polarization governed by the EOMFs $|\mathcal{B}^{\pm}_{\text{eff}}|$ results in the distinct conductance features that are related to the K and K' valleys, respectively.

The paper is organized as follows. We introduce the model and numerical methods employed in this work in Sec. II. In Sec. III, we talk about the low energy effective theory and introduce the concept of the EOMFs and CLLs. Section IV presents the key findings of our calculations and the corresponding remarks. More specifically, in Sec. IV A, we study the effect of the Anderson disorders and reveal the mechanisms driving the fragility of PLLs against disorders. Dephasing effect, which is covered in Sec. IV B, is another barrier to the robustness of the CLLs. Section IV C discussed

*zqbao@phy.ecnu.edu.cn
†qijj@baqis.ac.cn

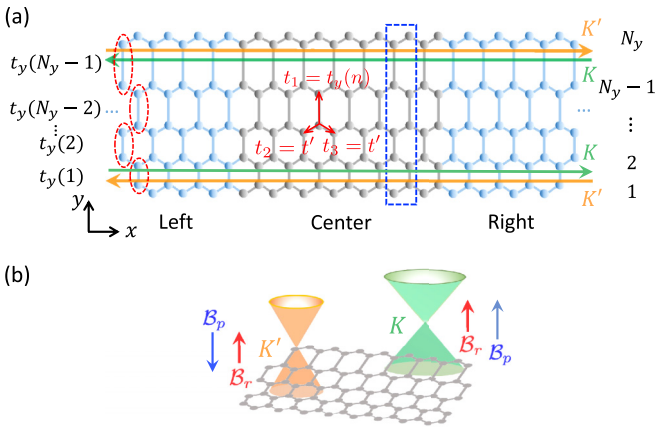

FIG. 1. (a) Schematic diagram of a two-terminal ZGNR with MIS. The gray (blue) colors represent the central region (leads). The size of the central region is set as N_y and N_x. The blue dotted rectangle represents a primitive cell, which contains $2N_y$ atoms. N_x is the number of primitive cells in the x direction. The green (orange) arrows depict the current for K (K') valley. (b) illustrates the K and K' valleys of the strained graphene with RMFs.

the tunability of the valley-polarized currents in the strained ZGNRs. Section V is the conclusion.

II. MODEL AND NUMERICAL METHODS

A two-terminal ZGNR with the MIS is illustrated in Fig. 1(a). The central region is sandwiched between the left (L) and right (R) leads. In realistic samples, Anderson disorders and dephasing effects are always present. In the following calculations, we suppose that the disorders and dephasing effects only exist in the central region. The dephasing effects are easily produced via electron-electron interactions, electron-phonon interactions, etc., and can be tuned by changing the temperature experimentally. Here, we simulate the dephasing effects by applying the Büttiker's virtual probe assumption [24]. The tight-binding Hamiltonian of the ZGNR with MIS in the central region can be written as

$$\mathcal{H} = \sum_i \varepsilon_i a_i^\dagger a_i - \sum_{\langle ij\rangle} t e^{i\phi_{ij}} a_i^\dagger a_j, \tag{1}$$

where ε_i represents the on-site energy, $a_i^\dagger$ and a_i represent the creation and annihilation operators, and $\langle ij\rangle$ sums over the nearest neighbors. In the L(R) leads, ε_i equals the Fermi energy E_F. In the central region, $\varepsilon_i = E_F + W$, where W denotes the disorder strength. Anderson disorders are simulated by the on-site energies that are uniformly distributed in $[-W/2, W/2]$. If RMFs exist, the hopping coefficient t should have a phase $\phi_{ij} = \int_i^j \mathbf{A}\cdot d\mathbf{l}/\phi_0$ with the vector potential $\mathbf{A}$ and the flux quantum $\phi_0 = \hbar/e$.

As shown in Fig. 1(a), we assume that the ZGNRs are only stretched along the y axis, with the hopping coefficient $t_y(n)$ being a linear function of n. For simplicity, $t_y(n)$ is defined as t_0 on the bottom edge and $t_0(1-\eta)$ on the top edge, respectively. $t_0 = -2.75$ eV is the well-known hopping coefficient for the normal graphene and η is an adjustable variable that reflects the strain strength. At any n, $t_y(n)$ can be expressed as $t_y(n) = t_0(1-\gamma n)$, where $\gamma = \frac{\eta(n-1)}{(N_y-2)n}$. Meanwhile, t_2 and t_3 are set as t_0. Specifically speaking, previous work stated that $t_y(n) = t_0\exp[-\beta(\ell_y(n)/a_0 - 1)]$ [19], where $\ell_y(n)$ is the corresponding bond length along the y direction, $a_0 = 0.142$ nm is the equilibrium bond length of the pristine graphene, and $\beta \approx 3.37$ is the decay rate. Consequently, $\eta = 0.5$ is corresponding to the maximum deformation strength 20% and it falls in the regime that is not destructive and reversible [16–19].

The conductance is calculated by combining the Landauer-Büttiker formula with the nonequilibrium Green function method at zero temperature [25–28]. The current in the real or virtual lead can be obtained by $I_p = (2e^2/h)\sum_{q\neq p} T_{pq}(E_F)(V_p - V_q)$, where $p = L, R, 1, 2, \ldots, N$, V_p is the bias in the lead p, and N is the number of lattice sites in the central region. Here, $T_{pq}(E_F) = \mathrm{Tr}[\Gamma_p(E_F)G^r(E_F)\Gamma_q(E_F)G^a(E_F)]$ is the transmission function at the Fermi energy E_F from lead q to lead p, and the line width function is given by $\Gamma_p(E_F) = i(\Sigma_p^r(E_F) - \Sigma_p^{r\dagger}(E_F))$. The retarded Green function is calculated by $G^r(E_F) = [G^a]^\dagger = [E_F I - H - \sum_p \Sigma_p^r(E_F)]^{-1}$, where $\Sigma_p^r(E_F)$ denotes the retarded self-energy associated with lead p. For the real lead, $\Sigma_{L/R}^r(E_F)$ can be calculated numerically [29]; for the virtual lead p, $\Sigma_p^r(E_F) = -id_p/2$, where d_p describes the dephasing strength [30,31]. To drive a current flowing along the x direction, a small bias $V = V_L - V_R$ is added between the L and R leads. Once the current I_L has been obtained, the conductance can be calculated directly by $G = (V_L - V_R)/I_L$. The average value of 500 random configurations is used to calculate the conductance.

III. LOW-ENERGY EFFECTIVE THEORY

For the strained ZGNR, the effective Hamiltonian is $\mathcal{H}^\pm(\boldsymbol{k}) = \boldsymbol{d}^\pm\cdot\boldsymbol{\sigma}$ [20], where

$$d_x^\pm = \hbar v_F\left(\pm k_x + r_\mp\frac{e\mathcal{B}_p y}{\hbar}\right),$$
$$d_y^\pm = \hbar v_F k_y\left(r_\pm - s_\pm\frac{e\mathcal{B}_p y}{\hbar}\right). \tag{2}$$

Here v_F is the Fermi velocity of the pristine graphene, $\pm$ represent K and K' valleys. $\mathcal{B}_p = \frac{\hbar\beta}{2ey}\varepsilon_{yy}$ is the PMF induced by the strain, $\varepsilon_{yy} = \partial_y u_y$ is the strain tensor, and u_y is the in-plane displacement of carbon atoms along the y direction [20,21]. $r_\pm = 1 \pm \frac{k_x}{2}$, $s_\pm = (\frac{3}{2} \pm \frac{k_x}{4})$, and we have set $a_0 = 1$. It should be pointed out that the Fermi velocities are modulated by the strain and should be anisotropic and momentum-dependent. By using the same method in Ref. [22], we can obtain the Fermi velocities of the carriers in the strained graphene $v_{Fx}^s = \frac{3t_0}{2}\sqrt{1 + \frac{2\gamma y}{3} - \frac{\gamma^2 y^2}{3}}$ and $v_{Fy}^s = \frac{3t_0}{2}(1-\gamma y)$.

In the presence of the RMFs, the canonical momentum should be replaced by the gauge invariant kinetic momentum,

thus the $\boldsymbol{d}$ vector changes to

$$d_x^{\pm} = v_F(\pm\Pi_x + r_{\mp}e\mathcal{B}_p y),$$
$$d_y^{\pm} = v_F\Pi_y\left(r_{\pm} - s_{\pm}\frac{e\mathcal{B}_p y}{\hbar}\right), \quad (3)$$

where $\Pi_i = p_i + e\mathcal{A}_{ri}$ $(i = x, y)$. Note that $r_{\pm}$ and $s_{\pm}$ contain k_x, thus $p_x = \hbar k_x$ in $r_{\pm}$ and $s_{\pm}$ should also be replaced by Π_x. However, the resulting additional terms in $r_{\pm}$ and $s_{\pm}$ can be neglected because they are smaller than other relevant terms. Thus, we obtain Eq. (3). For a perpendicular RMF, we choose the gauge $\mathcal{A}_{rx} = \mathcal{B}_r y$ and $\mathcal{A}_{ry} = 0$, then the Hamiltonian becomes

$$\mathcal{H}^{\pm} = v_F\left[\sigma_x(\pm p_x \pm e\mathcal{B}^{\pm}_{\text{eff}}y) + \sigma_y p_y\left(r_{\pm} - s_{\pm}\frac{e\mathcal{B}_p y}{\hbar}\right)\right], \quad (4)$$

where $\mathcal{B}^{\pm}_{\text{eff}} = \mathcal{B}_r \pm r_{\mp}\mathcal{B}_p$ is the EOMF which incorporates the effects of both the PMFs and RMFs. Note that $\mathcal{B}^{\pm}_{\text{eff}}$ is *not* the direct addition of $\mathcal{B}_r$ and $\mathcal{B}_p$, and $r_{\mp}$, the coefficient of $\mathcal{B}_p$, is dependent on k_x. This reflects the essential differences between the RMFs and PMFs, i.e., RMFs induce flat LLs, but PMFs induce dispersive ones.

By solving the eigenvalue equation

$$\mathcal{H}^{\pm}\begin{pmatrix}\psi_A(y)\\ \psi_B(y)\end{pmatrix} = \varepsilon_{\pm}\begin{pmatrix}\psi_A(y)\\ \psi_B(y)\end{pmatrix}, \quad (5)$$

where ψ_A and ψ_B are components for the A and B sublattices, we can obtain the bulk LLs $\varepsilon_{\pm}$. Using the similar method adopted in Ref. [20], we get

$$\varepsilon^2_{\pm} = 2ne\hbar v_F^2|\mathcal{B}^{\pm}_{\text{eff}}|\left(r_{\pm} + k_x s_{\pm}\frac{\mathcal{B}_p}{\mathcal{B}^{\pm}_{\text{eff}}}\right). \quad (6)$$

Because the orientations of the RMF and PMF are opposite for the K' valley, $\mathcal{B}^{-}_{\text{eff}} = \mathcal{B}_r - r_+\mathcal{B}_p$ might be zero. Thus, our solutions for the CLLs are invalid when $\mathcal{B}^{-}_{\text{eff}} = 0$. Actually, $\mathcal{B}^{-}_{\text{eff}} = 0$ is a critical point that the CLLs, as well as the edge currents for the K' valley vanish, which also can be illustrated in Fig. 2(c) and Fig. 7(b). Furthermore, the result of ε^2_- in the K' valley is invalid in the vicinity of the singular point $\mathcal{B}^{-}_{\text{eff}} = 0$. For more information, see the derivations and discussions in Appendix A.

IV. NUMERICAL RESULTS AND DISCUSSIONS

A. Anderson disorders

Next, we examine whether the valley currents in the strained ZGNRs are robust against static disorders. Figures 2(a)–2(e) illustrate the band structures with the strain strength $\eta = 0.5$. As discussed in Sec. III, the electrons in both valleys encounter the EOMFs $\mathcal{B}^{\pm}_{\text{eff}}$. When $\mathcal{B}_r = 0$, $\mathcal{B}^{\pm}_{\text{eff}}$ devolves to $\pm r_{\mp}\mathcal{B}_p$, producing the dispersive and symmetric PLLs in Fig. 2(a). If $\mathcal{B}_r$ is present, the directions of the RMF and PMF in the K (K') valley are the same (different). Therefore, $|\mathcal{B}^{-}_{\text{eff}}|$ keeps decreasing as $\mathcal{B}_r$ increases before $|\mathcal{B}^{-}_{\text{eff}}|$ reaches zero, and the CLLs become lower and narrower in the K' valley as shown in Fig. 2(b). The CLLs disappear when $|\mathcal{B}^{-}_{\text{eff}}| = 0$ in Fig. 2(c). If $\mathcal{B}_r$ keeps rising, $|\mathcal{B}^{-}_{\text{eff}}|$ gradually increases and the CLLs reappear in Fig. 2(d). Contrary to the K' valley, the CLLs in the K valley always become higher and wider because $|\mathcal{B}^{+}_{\text{eff}}|$ continues to grow as $\mathcal{B}_r$ increases.

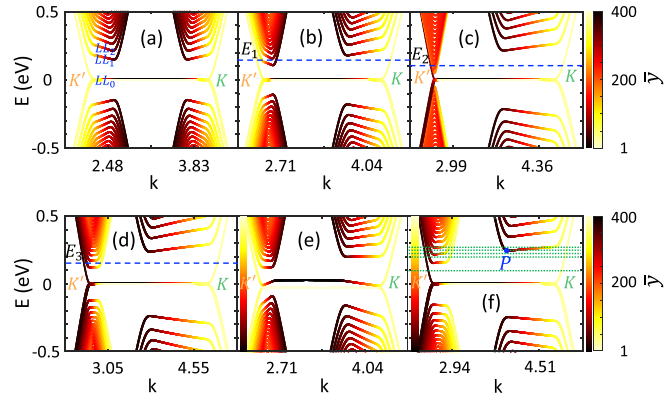

FIG. 2. (a)–(e) are dispersions for the ZGNR with MIS for $\eta = 0.5$. The RMF is $\mathcal{B}_r = 0$ in (a), $\mathcal{B}_r = 15\,\text{T}$ in (b), $\mathcal{B}_r = 35\,\text{T}$ in (c), and $\mathcal{B}_r = 50\,\text{T}$ in (d). $\mathcal{B}_r = 15\,\text{T}$ and $\mathcal{E}_y = 0.02t_0$ are adopted in (e). $\eta = 0.35$ and $\mathcal{B}_r = 50\,\text{T}$ are adopted in (f), in which the green dashed lines labeling several Fermi energies are used to analyze the conductance in Fig. 3. The color scale represents the expectation value of the y for each eigenstate. In all cases, we take N_y=200. Specifically, the colors in (a)–(d) and (f) predict the degenerate states at $E_F = 0$ are localized on both sizes of the sample. The blue dashed lines label the Fermi energy E_F in (b)–(d), which are used to illustrate the valley currents in Sec. IV C.

Figure 3(a) shows that only the first plateau is robust against Anderson disorders when $\mathcal{B}_r = 0$. The similar results have been obtained in previous work [32], where the authors attributed the robustness of the first plateau to the polarization of the sublattice. Figures 3(b)–3(d) illustrate the conductance with $\mathcal{B}_r = 15\,\text{T}$ ($\mathcal{B}^{-}_{\text{eff}} < 0$), $\mathcal{B}_r = 35\,\text{T}$ ($\mathcal{B}^{-}_{\text{eff}} \approx 0$), and $\mathcal{B}_r = 50\,\text{T}$ ($\mathcal{B}^{-}_{\text{eff}} > 0$), indicating that $\mathcal{B}_r$ can improve the robust performances because the higher plateaus become more robust. *Why are the edges states related to the PLLs not robust as that related to RLLs?* There are two main reasons for this. First, the counter-propagating modes with spatial overlap and close energies are easily hybridized leading to the enhancement of intervalley scattering. For the quantum Hall effect(QHE) as seen from Fig. 4(a), the bulk states are

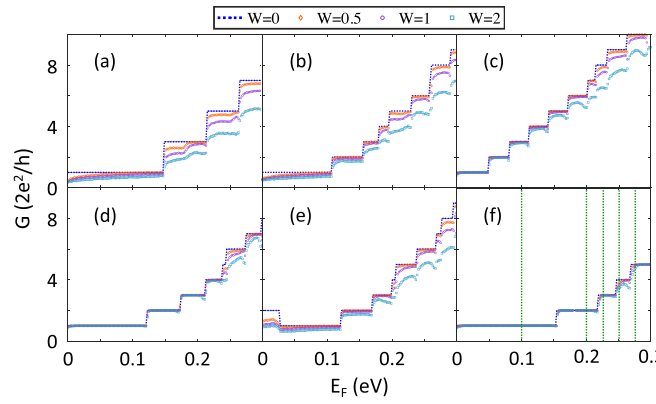

FIG. 3. (a)–(f) The conductance for the ZGNRs with MIS which are one-to-one correspondence with Figs. 2(a)–2(f). The green dashed lines in (f) correspond to those in the energy bands of Fig. 2(f). In all cases, we take $N_x = 30$ and $N_y = 200$.

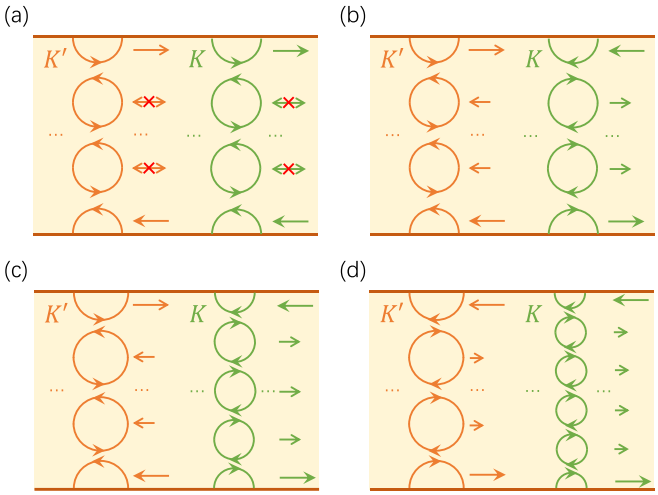

FIG. 4. The schematic bulk and edge states of (a) the QHE with the RMF $\mathcal{B}_r$, (b) the QVHE with the PMF $\mathcal{B}_p$, (c) the QVHE with both $\mathcal{B}_r = 15\,\mathrm{T}$ and $\mathcal{B}_p$, and (d) the QVHE with both $\mathcal{B}_r = 50\,\mathrm{T}$ and $\mathcal{B}_p$. The lengths of arrows represent the magnitudes of the group velocities, which are the slopes of the energy bands.

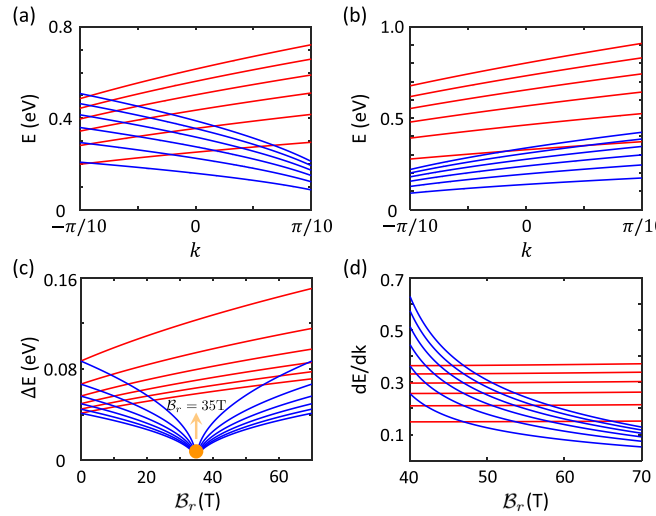

FIG. 5. (a)–(d) are plotted according to Eq. (6). The CLLs are shown in the vicinity of the K (red lines) and K' (blue lines) valleys with $\mathcal{B}_r = 15\,\mathrm{T}$ and $\mathcal{B}_r = 50\,\mathrm{T}$ in (a) and (b), respectively. (c) shows the energy spacing ΔE between several adjacent lowest CLLs versus $\mathcal{B}_r$ at the Dirac point. The small orange circle represents that $\mathcal{B}_r = 35\,\mathrm{T}$ is a singular point. (d) The slopes of the CLLs at the Dirac point.

localized because the group velocities are zero. The counter-propagating states are entirely separated by the bulk states on the two sides of the sample. Thus, the conductance plateaus in QHE are robust. According to Fig. 4(b), the degenerate counter-propagating states of PLLs overlap in space leading to the enhancement of the intervalley scattering, since the PMFs are opposite between the K and K' valleys due to the time-reversal symmetry. As a result, the conductance plateaus may not be robust due to hybridizations between the edge-edge states, the bulk-bulk states, and the edge-bulk states with spatial overlap. Additionally, since the counter-propagating modes cannot be spatially separated by the transverse electric field $\mathcal{E}_y$, the robustness in Fig. 3(e) cannot be considerably improved. It should be noted that the second plateau becomes more robust than it is in Fig. 3(a) due to the shift of the valley degeneracy.

Figures 4(c) and 4(d) illustrate the edge and bulk states of the quantum valley Hall effect(QVHE) when $\mathcal{B}_r$ and $\mathcal{B}_p$ both exist. In Fig. 4(c), $\mathcal{B}_r = 15\,\mathrm{T}$ and $\mathcal{B}_{\mathrm{eff}}^{-} < 0$, so $|\mathcal{B}_{\mathrm{eff}}^{-}|$ ($|\mathcal{B}_{\mathrm{eff}}^{+}|$) decreases (increases) and the cyclotron radius of the electrons in the K' and K valleys gets larger (smaller). Furthermore, The degeneracy of energies between the K and K' valleys has also been lifted, as shown in Fig. 2(b). There is only K' valley contributing to the transport, leading to the suppression of the intervalley scattering, especially for the low-energy regime. Even for higher energies, the states at the Fermi level are separated in real space when the Fermi energy crosses both valleys due to the asymmetry between the K and K' valleys. As a result, the conductance plateaus become more robust. Figure 4(d) show the case for a large $\mathcal{B}_r = 50\,\mathrm{T}$ and $\mathcal{B}_{\mathrm{eff}}^{-} > 0$. In this regime, $\mathcal{B}_{\mathrm{eff}}^{-}$ makes the electrons in the K' valley counterrotating. As a result, the directions of valley current for the two valleys coincide, further reducing hybridization and making the conductance plateaus more robust.

Second, the intravalley hybridization also has three origins: the bulk-bulk and edge-edge hybridizations are weak because they both flow in the same direction; the bulk-edge hybridization becomes important because the directions of the bulk and edge currents are opposite at least near one edge [see Figs. 4(b)–4(d)]. The bulk-edge hybridization can be affected by (i) the degeneracy of CLLs. The results of Figs. 5(a) and 5(b) demonstrate the valley polarization in the presence of $\mathcal{B}_r$ and are consistent with the bands in Figs. 2(b) and 2(d) derived from the tight-binding approach. Moreover, we plot the energy spacing of the CLLs at the Dirac points ($k_x = 0$) in Fig. 5(c). It can be seen that, in the K' valley, $|\mathcal{B}_{\mathrm{eff}}^{-}|$ and the energy spacing ΔE monotonically drops and grows as $\mathcal{B}_r$ increases when $\mathcal{B}_r < 35\,\mathrm{T}$ and $\mathcal{B}_r > 35\,\mathrm{T}$, respectively. In the K valley, $|\mathcal{B}_{\mathrm{eff}}^{+}|$ always grows as $\mathcal{B}_r$ increases. Hence, ΔE between neighboring CLLs keeps increasing. If $|\mathcal{B}_{\mathrm{eff}}^{+}|$ is larger, the cyclotron radius in the K valley is smaller, resulting in more bulk states that can be hybridized with the edge states. (ii) The slopes of the dispersive CLLs, shown in Fig. 5(d), characterize the nonzero group velocities that can take part in electronic transport. The counter-propagating modes with larger group velocities may lead to stronger scattering. It should be noted that only the $\mathcal{B}_r > 40\,\mathrm{T}$ regime is depicted in Fig. 5(d) because $\mathcal{B}_r = 35\,\mathrm{T}$ ($\mathcal{B}_{\mathrm{eff}}^{-} = 0$) is a singular point and we address the situation in the $\mathcal{B}_{\mathrm{eff}}^{-} > 0$ regime at this time. For the intravalley scattering, the bulk and edge states related to the dispersive PLLs will inevitably hybridize because it is easier for the Fermi energy to cross both the bulk and edge states at once.

Quite interestingly, the seventh plateau is more robust than the sixth plateau in Fig. 3(d). In order to explore this phenomenon, we choose another set of parameters $\eta = 0.35$ and $\mathcal{B}_r = 50\,\mathrm{T}$ in Fig. 3(f) and obtain similar results that the fifth plateau is more robust than the fourth plateau. The green dashed lines plotted in Fig. 2(f) are one-to-one correspondence with those in Fig. 3(f). The corresponding relations indicate that the fourth plateau is fragile because E_F crosses the first CLL (bulk states) in the K valley; however, the

higher fifth plateau is still robust because only edge states are crossed by E_F in the K valley. The hybridization between the counter-propagating modes around P [see Fig. 2(f)] with close distance in space features the fragility of the fourth plateau. The behaviors exhibit the polarization of the K and K' valleys, which are determined by the EOMFs $|\mathcal{B}^{\pm}_{\text{eff}}|$. In our work, the valley polarization has three major aspects: the shift of valley degeneracy, the degeneracy of CLLs, and the slopes of CLLs (group velocities) in the K and K' valleys. The mechanisms of the intervalley and intravalley scattering revealed by the preceding paragraphs make the different transport behaviors of PLLs and RLLs clear. On this basis, valley polarization determined by the EOMFs $|\mathcal{B}^{\pm}_{\text{eff}}|$ uncovers the different performances of conductance which are related to the K and K' valleys, respectively.

Furthermore, it should be pointed out that despite the presence of RMFs in Figs. 3(b)–3(f), the higher plateaus are still not as robust as the ones in the QHE. On one hand, the CLLs are broadened when the disorder is present. On the other hand, the direct energy spacing ΔE between two adjacent higher CLLs becomes smaller. Thus, the direct gap between two adjacent CLLs can be smeared out due to the broadening of these states by the disorder. In this regime, bulk-bulk hybridization also plays a role in transport properties. Note that the Rashba spin-orbit coupling (RSOC) and Zeeman energy are not included throughout the work because it has no impact on our understanding of physics (See Appendix B for more information).

B. Dephasing effects

Aside from the static impurities, dephasing is another significant impediment to robust performance. Then we look at the dephasing effects in the ZGNRs with MIS. The coherent length L_ϕ is a measure of coherence in experiments. Electrons can go from the left lead to the right lead directly or via the virtual leads in the presence of dephasing effects, resulting in coherent and incoherent currents, respectively. At a certain dp, the incoherent current grows as the length N_x does as well. When the coherent and incoherent parts of the current are equal, N_x is the coherent length L_ϕ [31]. Note that L_ϕ is an average value of the ZGNRs with MIS. The carbon-carbon distance in our model is not uniform along the y axis. The real L_ϕ along the edge may be less than our numerical value. L_ϕ changes with dp for three distinct cases of EOMFs: PLLs, CLLs, and RLLs are shown in Fig. 6(a). At a specific dp, the value of L_ϕ is the lowest for PLLs. That means dephasing effects are more sensitive to PMFs. The reason is that strain modifies the bond length between carbon atoms in the ZGNRs, and the dephasing effects caused by electron-phonon and electron-electron interactions are amplified [33,34]. However, the cases of EOMFs ($\mathcal{B}_r \neq 0$) improve the value of L_ϕ in an obvious way. Because of the weakening of the hybridization demonstrated in Sec. IV A, it can be concluded that the addition of RMFs considerably increases the sample's robustness against dephasing effects.

In Fig. 6(b), we examine the conductance of the CLLs ($\mathcal{B}_r = 50\,\text{T}$) under various dp. In the weak and moderate dephasing regime ($dp < 0.2\,\text{eV}$), the conductance related to the lowest two CLLs are very robust due to the suppression of

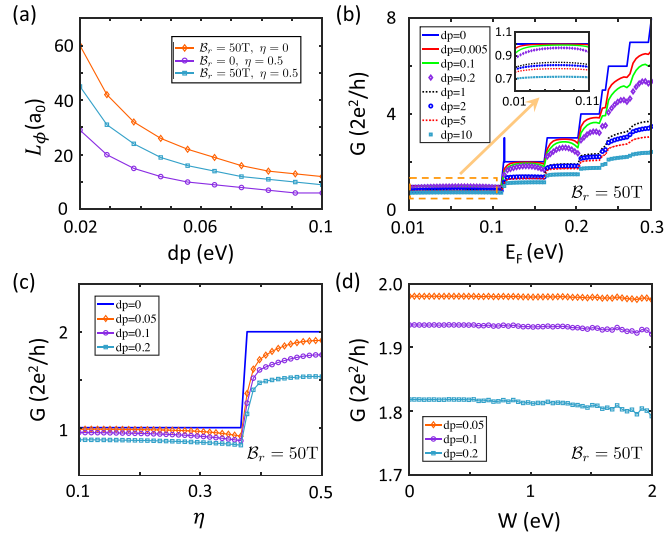

FIG. 6. (a) The coherent length L_ϕ vs the dephasing strength dp for various EOMFs with $E_F = 0.2\,\text{eV}$. The conductance G vs (b) the Fermi energy E_F, (c) the strain strength η, and (d) the disorder strength W for various dp, respectively. We set $\eta = 0.5$ in (b) and (d), $E_F = 0.15\,\text{eV}$ in (c) and (d), and $\mathcal{B}_r = 50\,\text{T}$ in (b)–(d). $N_y = 200$ in all case. We take $N_x = 30$ in (c) and $N_x = 12$ in other cases.

hybridization. However, the ones with higher CLLs are not robust. This is due to the broadening of the higher CLLs brought on by the dephasing effects. In the higher CLLs, the spacing between adjacent energy levels gets smaller. Thus, the hybridization is again intensified. In the strong dephasing regime ($dp \geqslant 1\,\text{eV}$), the conductance exhibits a quasi-quantization with $G \lesssim 1\,\text{eV}$. This outcome is in line with earlier research [35,36]. According to Fig. 6(c), the plateau of conductance gradually dissipates as the strain strength η increases. The result is consistent with the performance of L_ϕ in Fig. 6(a). Finally, we consider the combination of Anderson disorder and dephasing effects in Fig. 6(d). The findings demonstrate that when disorder strength W grows, conductance value marginally reduces under various dp.

The results above show that tunable valley currents of the low CLLs are robust against dephasing effects when $\mathcal{B}_r \neq 0$. The edge states related to higher CLLs are not robust, though. Examining Hall conductance or developing novel solutions may be required as a next step to improve the performance of tuning valley currents against dephasing effects.

C. Tunability of the valley-polarized currents

The tunability of the valley-polarized currents in our system allows for the construction of new types of useful valleytronic devices. The band structures in Figs. 2(b)–2(f) clearly demonstrate that the different EOMFs between the K and K' valleys induce the valley polarization. The valley currents depicted in Figs. 7(a)–7(c) correspond to the states at Fermi energies E_1–E_3 in Figs. 2(b)–2(d). The edge states are significantly out of balance between the K and K' valleys, which differ greatly from that of the well-known QHE, quantum spin Hall effects (QSHE), and QVHE. Therefore, our sample is a good platform for manufacturing valleytronic devices by tuning E_F, RMFs, or PMFs.

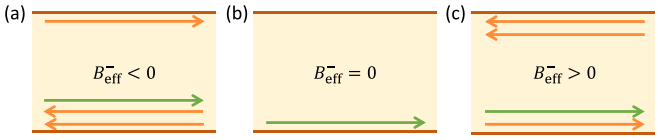

FIG. 7. The edge valley currents for (a) $\mathcal{B}^-_{\rm eff} < 0$, (b) $\mathcal{B}^-_{\rm eff} = 0$, and (c) $\mathcal{B}^-_{\rm eff} > 0$. The orange lines and green lines represent the currents in the K' and K valleys, respectively.

We may generalize our tunability of the valley-polarized currents to the ZGNRs with symmetric strain (SS) [23]. As shown in Fig. 8(a), the ZGNRs with SS can be viewed as two reverse copies of the ZGNR with MIS, and snake states exist in the middle of the sample. Figure 8(b) depicts the band structure of the ZGNR with SS, and previous work has demonstrated that without the RMFs, only the first plateau is robust against the Anderson disorders. If we apply a RMF $\mathcal{B}_r = 50\,\mathrm{T}$, the CLLs are shown in Fig. 8(c), and as illustrated in Fig. 8(d), the higher plateaus related to the snake states are extremely robust against the Anderson disorders. In the presence of the dephasing effects, the plateaus of snake states are very robust for the first CLL and survive for the higher CLLs. Therefore, the results of the ZGNRs with SS are similar to that of the ZGNRs with MIS in Sec. IV A and Sec. IV B. To sum up, snake states can survive for both Anderson disorders and dephasing effects which show excellent design potential for new quantum devices.

V. CONCLUSIONS

In this work, we investigate the strained ZGNRs in the presence of the RMFs. The essential distinction between the RLLs and PLLs which are produced by the RMFs and PMFs, respectively, is that the former are flat while the latter are dispersive. Because of their dispersive nature, the PLLs are susceptible to disorders because of the hybridization of their bulk and edge states. In order to incorporate the effects of the RMFs and PMFs, the concept of the EOMFs is introduced. Accordingly, we obtain the CLLs which combine the RLLs and PLLs. Then we examine the robust behaviors of the valley-polarized currents by calculating the conductance and discover that the RMF can improve the robust performances. Our transport calculations of the K and K' valleys demonstrate distinctive robust behaviors against the Anderson disorders and dephasing effect. The several mechanisms of the intervalley and intravalley scattering make it clear how PLLs and RLLs behave differently on transport properties. Moreover, the valley polarization induced by the EOMFs $|\mathcal{B}^\pm_{\rm eff}|$ reveals the distinct conductance performances that are related to the K and K' valleys, respectively. The behaviors of the conductance G show that the RMF $\mathcal{B}_r$ is a valid tool for tuning the valley currents. Furthermore, we investigate the tunability of the valley-polarized currents in the ZGNRs with MIS and SS, respectively. We discover that our polarized edge states differ greatly from the well-known QHE, QSHE, and QVHE. Because of their efficient tunability, they are ideal for designing new sorts of valleytronics devices.

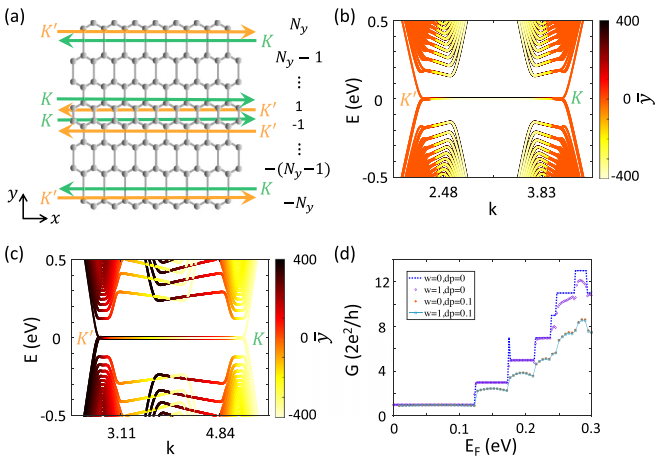

FIG. 8. (a) The schematic diagram of the ZGNRs with SS. (b) and (c) illustrate the band structures with $\mathcal{B}_r = 0$ and $\mathcal{B}_r = 50\,\mathrm{T}$, respectively. (d) The conductance G vs the Fermi energy E_F for various W and dp with $\mathcal{B}_r = 50\,\mathrm{T}$. In all cases, we set $N_x = 30$, $N_y = 400$, and $\eta = 0.5$.

ACKNOWLEDGMENTS

The authors would like to thank Qing-feng Sun, Shuai Zhao, Yanxia Xing, and Hua Jiang for helpful discussions. We are grateful to the National Natural Science Foundation of China (Grant No. 12204053), the Natural Science Foundation of Shanghai (Grant No. 21JC1402300), and Director's Fund of Key Laboratory of Polar Materials and Devices, Ministry of Education.

APPENDIX A: THE SOLUTIONS OF THE CLLs

In this section, we use the similar method adopted in Ref. [20] to derive the expressions of CLLs. The Hamiltonian for the K valley is shown in Eq. (4) in the main text:

$$\boldsymbol{d}^+ \cdot \boldsymbol{\sigma} = v_F(p_x + e\mathcal{B}^+_{\rm eff} y)\sigma_x - i\hbar v_F\left(r_+ - s_+ \frac{e\mathcal{B}_p y}{\hbar}\right)\partial_y \sigma_y. \tag{A1}$$

We can shift y to $y + \frac{\hbar r_+}{e\mathcal{B}_p s_+}$ and hermitize $-iy\partial_y$ to $-i(y\partial_y + \frac{1}{2})$, then Eq. (A1) becomes

$$\boldsymbol{d}^+ \cdot \boldsymbol{\sigma} = \hbar v_F \begin{pmatrix} 0 & h^+_+ \\ h^+_- & 0 \end{pmatrix}, \tag{A2}$$

where

$$h^+_\pm = \left[k_x + \frac{e\mathcal{B}^+_{\rm eff}}{\hbar}\left(y + \frac{\hbar r_+}{e\mathcal{B}_p s_+}\right)\right] \pm s_+ \frac{e\mathcal{B}_p}{\hbar}\left(y\partial_y + \frac{1}{2}\right). \tag{A3}$$

Thus the eigenvalue equations for the K valley [Eq. (5) in the main text] become

$$\left[k_x + \frac{e\mathcal{B}^+_{\rm eff}}{\hbar}\left(y + \frac{\hbar r_+}{e\mathcal{B}_p s_+}\right) + s_+ \frac{e\mathcal{B}_p}{\hbar}\left(y\partial_y + \frac{1}{2}\right)\right]\psi_B = \varepsilon\psi_A,$$
$$\left[k_x + \frac{e\mathcal{B}^+_{\rm eff}}{\hbar}\left(y + \frac{\hbar r_+}{e\mathcal{B}_p s_+}\right) - s_+ \frac{e\mathcal{B}_p}{\hbar}\left(y\partial_y + \frac{1}{2}\right)\right]\psi_A = \varepsilon\psi_B. \tag{A4}$$

Eliminating ψ_A, we can obtain

$$\left[\left(\frac{e\mathcal{B}^+_{\rm eff}}{\hbar}y\right)^2+\frac{e\mathcal{B}^+_{\rm eff}}{\hbar s_+}\left(2k_xs_++2r_+\frac{\mathcal{B}^+_{\rm eff}}{\mathcal{B}_p}-\frac{e\mathcal{B}_p}{\hbar}s_+^2\right)y+\frac{\Delta}{s_+^2}-\frac{e^2\mathcal{B}_p^2s_+^2}{4\hbar^2}\right]\psi_B-\frac{e^2\mathcal{B}_p^2}{\hbar^2}s_+^2(2y\psi_B'+y^2\psi_B'')=0, \tag{A5}$$

where

$$\Delta=\left(k_xs_++\frac{r_+\mathcal{B}^+_{\rm eff}}{\mathcal{B}_p}\right)^2-s_+^2\varepsilon^2. \tag{A6}$$

Two singularities of Eq. (A5) are 0 and ∞. Toward 0, Eq. (A5) can be asymptotically expressed as

$$\left(\frac{\Delta}{s_+^2}-\frac{e^2\mathcal{B}_p^2s_+^2}{4\hbar^2}\right)\psi_B-\frac{e^2\mathcal{B}_p^2}{\hbar^2}s_+^2(2y\psi_B'+y^2\psi_B'')=0. \tag{A7}$$

Equation (A7) has two independent solutions $y^{-\frac{1}{2}\mp\frac{\hbar\sqrt{\Delta}}{e|\mathcal{B}_p|s_+^2}}$, however, because we consider the asymptotic solution toward 0, only $y^{-\frac{1}{2}+\frac{\hbar\sqrt{\Delta}}{e|\mathcal{B}_p|s_+^2}}$ is acceptable. Toward ∞, Eq. (A5) is asymptotically expressed as

$$\left(\frac{e\mathcal{B}^+_{\rm eff}}{\hbar}y\right)^2\psi_B-\left(\frac{e\mathcal{B}^+_{p}}{\hbar}s_+y\right)^2\psi_B''=0, \tag{A8}$$

and the asymptotic solution can be written as $e^{-\frac{z}{2}}$, where

$$z=-{\rm sgn}(\mathcal{B}_p)\frac{2}{s_+}\left|\frac{\mathcal{B}^+_{\rm eff}}{\mathcal{B}_p}\right|y. \tag{A9}$$

Note that Eq. (A9) differs from the asymptotic solution in Ref. [20] which solely contains PMFs. In conclusion, the general solution of Eq. (A5) can be written as

$$\psi_B(y)=e^{-\frac{z}{2}}y^{-\frac{1}{2}+\frac{\hbar\sqrt{\Delta}}{e|\mathcal{B}_p|s_+^2}}u(y). \tag{A10}$$

Substituting Eq. (A10) into Eq. (A5), and changing the variable from y to z, we can obtain the equation

$$zu''(z)+(\xi-z)u'(z)-\alpha u(z)=0, \tag{A11}$$

where

$$\xi=1+\frac{2\hbar\sqrt{\Delta}}{e|\mathcal{B}_p|s_+^2},$$
$$\alpha=\frac{\sqrt{\Delta}-k_xs_+{\rm sgn}(\mathcal{B}_p\mathcal{B}^+_{\rm eff})-r_+\left|\frac{\mathcal{B}^+_{\rm eff}}{\mathcal{B}_p}\right|}{e|\mathcal{B}_p|s_+^2/\hbar}+\frac{(\mathcal{B}^+_{\rm eff}+|\mathcal{B}^+_{\rm eff}|)s_+^2}{2|\mathcal{B}^+_{\rm eff}|s_+^2}. \tag{A12}$$

Equation (A11) is a confluent hypergeometric equation, and α must be a nonpositive integer to guarantee that the solution is convergent. Thus, $\alpha=-n$ leads to the CLLs

$$\varepsilon_+^2=ne\hbar v_F^2|\mathcal{B}^+_{\rm eff}|\left(2k_xs_+\frac{\mathcal{B}_p}{\mathcal{B}^+_{\rm eff}}+2r_+-n\frac{e\mathcal{B}_p^2}{\hbar|\mathcal{B}^+_{\rm eff}|}s_+^2\right). \tag{A13}$$

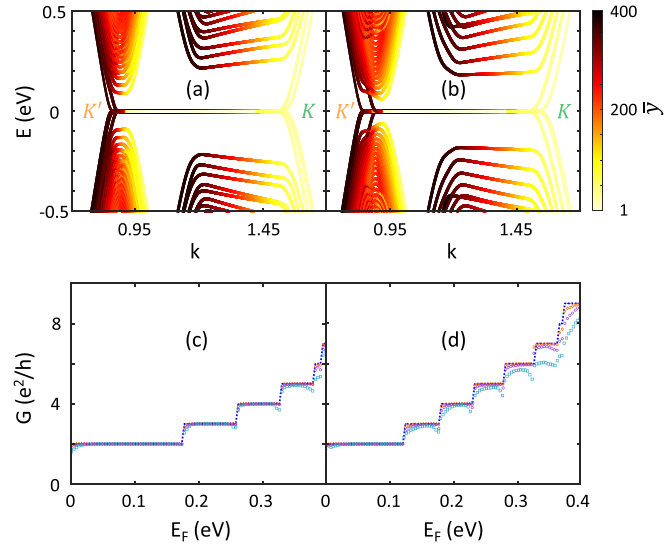

FIG. 9. (a) and (b) show the band structures with the RSOC strength $V_R=0.02t$ and $V_R=0.05t$, respectively. (c) and (d) are the conductance corresponding to (a) and (b). In all cases, we set $\mathcal{B}_r=50\,$T and $\eta=0.5$. In all cases, $N_x=30$ and $N_y=200$.

Because the third term is small, we can neglect it and obtain

$$\varepsilon_+^2=2ne\hbar v_F^2|\mathcal{B}^+_{\rm eff}|\left(r_++k_xs_+\frac{\mathcal{B}_p}{\mathcal{B}^+_{\rm eff}}\right). \tag{A14}$$

Similarly, the CLLs for the K' valley are

$$\varepsilon_-^2=2ne\hbar v_F^2|\mathcal{B}^-_{\rm eff}|\left(r_-+k_xs_-\frac{\mathcal{B}_p}{\mathcal{B}^-_{\rm eff}}\right). \tag{A15}$$

It should be pointed out that $\mathcal{B}^-_{\rm eff}=\mathcal{B}_r-r_+\mathcal{B}_p$ can be zero because the directions of the RMF and PMF are opposite for the K' valley. Actually, α for the K' valley has the singular point $\mathcal{B}^-_{\rm eff}=0$; as a result, our solutions for the CLLs are invalid when the EOMF $\mathcal{B}^-_{\rm eff}=0$. Furthermore, ε_-^2 in Eq. (A15) may be negative if the absolute value of $\mathcal{B}^-_{\rm eff}$ is a small value. Therefore, our result for ε_- is invalid in the vicinity of the singular point $\mathcal{B}^-_{\rm eff}=0$.

APPENDIX B: RASHBA SPIN-ORBIT COUPLING

We investigate the ZGNRs with MIS for various RSOC strengths V_R. It should be pointed out that since the RSOC breaks the spin degeneracy, we take into account the spin degree of freedom in this part. The band structures and conductance for $V_R=0.02t$ and $V_R=0.05t$ are shown in Fig. 9, demonstrating that the conductance are still quantized even if the RSOC causes the extended states. Additionally, odd plateaus appear as a result of the RSOC lifting the spin degeneration. Due to the existence of the RMFs, both the odd and even plateaus are robust against Anderson disorder. As a result, the RSOC does not invalidate the primary findings in the main paper. Additionally, we ignore the Zeeman energy in our calculations because it is negligibly small and only splits the energy band, having no impact on the physics discussed in this paper.

[1] A. H. Castro Neto, F. Guinea, N. M. R. Peres, K. S. Novoselov, and A. K. Geim, The electronic properties of graphene, Rev. Mod. Phys. **81**, 109 (2009).

[2] A. Rycerz, J. Tworzydo and C. W. J. Beenakker, Valley filter and valley valve in graphene, Nat. Phys. **3**, 172 (2007).

[3] S. P. Milovanović and F. M. Peeters, Strain controlled valley filtering in multi-terminal graphene structures, Appl. Phys. Lett. **109**, 203108 (2016).

[4] Z. Yu, F. Xu, and J. Wang, Valley Seebeck effect in gate tunable zigzag graphene nanoribbons, Carbon **99**, 451 (2016).

[5] W.-Y. He and L. He, Coupled spin and pseudomagnetic field in graphene nanoribbons, Phys. Rev. B **88**, 085411 (2013).

[6] F. Guinea, M. I. Katsnelson, and A. K. Geim, Energy gaps and a zero-field quantum Hall effect in graphene by strain engineering, Nat. Phys. **6**, 30 (2010).

[7] T. Low and F. Guinea, Strain-induced pseudomagnetic field for novel graphene electronics, Nano Lett. **10**, 3551 (2010).

[8] M. A. H. Vozmediano, M. I. Katsnelson, and F. Guinea, Gauge fields in graphene, Phys. Rep. **496**, 109 (2010).

[9] S. Zhu, J. A. Stroscio, and T. Li, Programmable Extreme Pseudomagnetic Fields in Graphene by a Uniaxial Stretch, Phys. Rev. Lett. **115**, 245501 (2015).

[10] D. Sabsovich, M. W. Bockrath, K. Shtengel, and E. Sela, Helical superconducting edge modes from pseudo-Landau levels in graphene, Phys. Rev. B **103**, 094513 (2021).

[11] J. Sun, T. Liu, Y. Du, and H. Guo, Strain-induced pseudomagnetic field in $\alpha - \mathcal{T}_3$ lattice, Phys. Rev. B **106**, 155417 (2022).

[12] N. Levy, S. A. Burke, K. L. Meaker, M. Panlasigui, A. Zettl, F. Guinea, A. H. C. Neto, and M. F. Crommie, Strain-induced pseudomagnetic fields greater than 300 tesla in graphene nanobubbles, Science **329**, 544 (2010).

[13] Y. Liu, J. N. B. Rodrigues, Y. Z. Luo, L. Li, A. Carvalho, M. Yang, E. Laksono, J. Lu, Y. Bao, H. Xu, S. J. R. Tan, Z. Qiu, C. H. Sow, Y. P. Feng, A. H. C. Neto, S. Adam, J. Lu, and K. P. Loh, Tailoring sample-wide pseudo-magnetic fields on a grapheneblack phosphorus heterostructure, Nat. Nanotechnol. **13**, 828 (2018).

[14] P. Nigge, A. C. Qu, É. Lantagne-Hurtubise, E. Mårsell, S. Link, G. Tom, M. Zonno, M. Michiardi, M. Schneider, S. Zhdanovich, G. Levy, U. Starke, C. Gutiérrez, D. Bonn, S. A. Burke, M. Franz, and A. Damascelli, Room temperature strain-induced Landau levels in graphene on a wafer-scale platform, Sci. Adv. **5**, eaaw5593 (2019).

[15] S.-Y. Li, Y. Su, Y.-N. Ren, and L. He, Valley Polarization and Inversion in Strained Graphene via Pseudo-Landau Levels, Valley Splitting of Real Landau Levels, and Confined States, Phys. Rev. Lett. **124**, 106802 (2020).

[16] E. Cadelano, P. L. Palla, S. Giordano, and L. Colombo, Non-Linear Elasticity of Monolayer Graphene, Phys. Rev. Lett. **102**, 235502 (2009).

[17] C. Lee, X. Wei, J. W. Kysar, and J. Hone, Measurement of the elastic properties and intrinsic strength of monolayer graphene, Science **321**, 385 (2008).

[18] F. Liu, P. Ming, and J. Li, Ab initio calculation of ideal strength and phonon instability of graphene under tension, Phys. Rev. B **76**, 064120 (2007).

[19] I. Yu. Sahalianov, T. M. Radchenko, V. A. Tatarenko, G. Cuniberti, and Y. I. Prylutskyy, Straintronics in graphene: Extra large electronic band gap induced by tensile and shear strains, J. Appl. Phys. **126**, 054302 (2019).

[20] É. Lantagne-Hurtubise, X.-X. Zhang, and M. Franz, Dispersive Landau levels and valley currents in strained graphene nanoribbons, Phys. Rev. B **101**, 085423 (2020).

[21] V. M. Pereira, A. H. C. Neto, and N. M. R. Peres, Tight-binding approach to uniaxial strain in graphene, Phys. Rev. B **80**, 045401 (2009).

[22] B.-L. Wu, Q. Wei, Z.-Q. Zhang, and H. Jiang, Transport property of inhomogeneous strained graphene, Chin. Phys. B **30**, 030504 (2021).

[23] C.-y. Zuo, J. Qi, T.-l. Lu, Z.-q. Bao, and Y. Li, Reverse strain-induced snake states in graphene nanoribbons, Phys. Rev. B **105**, 195420 (2022).

[24] M. Büttiker, Role of quantum coherence in series resistors, Phys. Rev. B **33**, 3020 (1986).

[25] R. Landauer, Electrical resistance of disordered one-dimensional lattices, Philos. Mag. **21**, 863 (1970).

[26] D. S. Fisher, and P. A. Lee, Relation between conductivity and transmission matrix, Phys. Rev. B **23**, 6851(R) (1981).

[27] Y. Meir and N. S. Wingreen, Landauer Formula for the Current Through An Interacting Electron Region, Phys. Rev. Lett. **68**, 2512 (1992).

[28] A.-P. Jauho, N. S. Wingreen, and Y. Meir, Time-dependent transport in interacting and noninteracting resonant-tunneling systems, Phys. Rev. B **50**, 5528 (1994).

[29] M. P. L. Sancho, J. M. L. Sancho and J. Rubio, Highly convergent schemes for the calculation of bulk and surface Green functions, J. Phys. F: Met. Phys. **15**, 851 (1985).

[30] H. Jiang, S. Cheng, Q.-f. Sun, and X. C. Xie, Topological Insulator: A New Quantized Spin Hall Resistance Robust to Dephasing, Phys. Rev. Lett. **103**, 036803 (2009).

[31] Y. Xing, Q.-f. Sun, and J. Wang, Influence of dephasing on the quantum Hall effect and the spin Hall effect, Phys. Rev. B **77**, 115346 (2008).

[32] M. Settnes, J. H. Garcia, and S. Roche, Valley-polarized quantum transport generated by gauge fields in graphene, 2D Mater. **4**, 031006 (2017).

[33] M. B. Lundeberg and J. A. Folk, Rippled Graphene in an In-Plane Magnetic Field: Effects of a Random Vector Potential, Phys. Rev. Lett. **105**, 146804 (2010).

[34] R. Burgos, J. Warnes, Leandro R. F. Lima, and C. Lewenkopf, Effects of a random gauge field on the conductivity of graphene sheets with disordered ripples, Phys. Rev. B **91**, 115403 (2015).

[35] Y. Shimomura and Y. Takane, Dephasing-Induced Stabilization of a Perfectly Conducting Channel in Disordered Graphene Nanoribbons with Zigzag Edges, J. Phys. Soc. Jpn. **85**, 014704 (2016).

[36] J.-C. Chen, H. Zhang, S.-Q. Shen and Q.-f. Sun, Dephasing effect on transport of a graphene pn junction in a quantum Hall regime, J. Phys.: Condens. Matter **23**, 495301 (2011).